Fullerene-Tetrabenzofluorene (C_{60}-TBF) in Multivalent Photosensitisation for Enhanced ZnO-based Photo-catalysts: Mono *vs.* Hexakis Adduct†

Munusamy Krishnamurthy,[#,a,b,c] Philip A. Hope,[#b] Periyamuthu Ramar,[a,c] A.A. Boopathi,[a,c] Srinivasan Sampath,[d*] Marc K. Etherington,[f] Alyssa-Jennifer Avestro[*b,e] Debasis Samanta[*a,c]

[a]*Polymer Science & Technology Department, CSIR–CLRI, Adyar, Chennai 600020, India.* [b]*Department of Chemistry, Durham University, Durham, DH1 3LE, UK.* [c]*Academy of Scientific and Innovative Research (AcSIR).* [d]*Department of Materials Science, School of Technology, Central University of Tamil Nadu, Thiruvarur 610101, India.* [e]*Department of Chemistry, University of York, York, YO10 5DD, UK.* [f]*Department of Physics, Durham University, South Road, Durham, DH1 3LE; Department of Mathematics, Physics & Electrical Engineering, Northumbria University, Ellison Place, Newcastle upon Tyne, NE1 8ST*

#Equal contributions

*Corresponding author e-mail addresses:

srinivasansampath@cutn.ac.in, alyssajennifer.avestro@york.ac.uk, debasis@clri.res.in

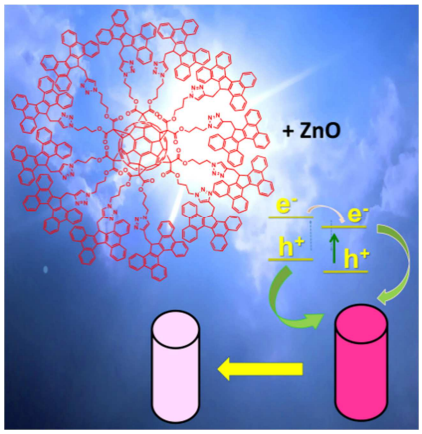

Photo-catalysts offer a simple catalytic method with widespread applications like degradation of polluting dyes, hydrogen generation from water, etc., in the presence of a photon source like sunlight. The development of a second-generation photo-catalyst in the form of a nanocomposite is an integral part of research to improve the practical usefulness and efficiency of the process. A systematic study using the active material with controlled functional groups is required to understand the process in detail as well as to develop efficient photocatalytic systems. In this paper, we report the design, synthesis, detailed physicochemical studies, and self-assembly of interesting materials where fullerenes have been functionalized with polycyclic, aromatic, conjugated, butterfly-shaped molecules like Tetrabenzofluorene (TBF) using a well-known click chemistry approach. Detailed analyses using spectroscopic, electrochemical, and microscopic or X-ray diffraction (single crystal) techniques were undertaken for a clear understanding of their photophysical or self-assembly behavior. The functionalized fullerene material was mainly used so that comparative results could be presented where two units (mono adduct) or twelve units (hexakis adduct) of TBF molecules were attached separately. These comparative studies were beneficial for unambiguous interpretation of results and drawing definitive conclusions regarding the energy transfer with cascade-type systems. Finally, those results were useful for the logical understanding of photo-catalytic experiments using those designer fullerene materials.

1. INTRODUCTION

Solar energy applications have gained considerable momentum over the years due to their potential to address several environmental and energy issues utilizing an abundant natural resource. In particular, the efficient photodegradation of organic dye pollutants using natural sunlight has direct implications for managing contaminated wastewater generated by global chemical, textile, and leather industries.[1] Historically, metal oxide semiconductors have dominated trends in solar energy technologies, including light-harvesting photovoltaics, photo-catalysts.[2] Development of efficient photo-catalyst is an integral part of research for effective degradation of polluting dyes. Various semiconducting metal oxides, particularly zinc oxides (ZnO), can degrade different organic dye compounds.[3-4] In this case, the semiconducting material absorbs light to excite electrons and produce holes, both of which can facilitate generating various active free radical species responsible for degradation of organic dyes to mostly non-harmful carbon dioxide, water, etc. Generally, the efficiency of photocatalytic reaction depends on the charge separation rate of electrons and holes, recombination rate of that photoexcited charges of semiconducting material. Hence, inhibition (or) controlling the recombination of electron-hole pairs of photocatalytic material is significant to increase the photo-catalyst efficiency.[5] However, pristine ZnO provides low photocatalytic activity due to high rate of charge recombination and large band gap.[6, 7] It was observed that the combination of metal oxide with organic, polymeric or carbon nanomaterials-based semiconductors is the effective strategy to enhance the photo-catalytic quantum efficiency.[8, 9] In this case, like bulk heterojunction solar cell devices, the electrons/holes can be transferred from one semiconducting material to the other preventing the recombination process. In this context, fullerene has been emerged as the material of choice as an electron acceptor due to its high electron mobility, excellent thermal stability, and outstanding charge transport characteristics with a bandgap of ~1.6-1.9 eV, hence has been used frequently in photovoltaic device[10,11]and other energy transfer devices.[12] Recently, the influences of fullerene on photo-catalytic performance have been studied.[13-15] Hongbo *et al.* reported that the fullerene hybridized zinc oxide surface enhances the degree of photocatalytic activity; fullerene not only helps to obtain higher efficiency and also provides photostability to the ZnO surface.[16] However, in most of the cases, pure fullerene directly used for the preparation of hybrid composites with zinc oxide limits the light absorbance potential and causes the nanoscale aggregation in an aqueous medium, decreasing the photocatalytic activity.[17] The incorporation of rigid π-conjugated aromatic moieties on fullerene surfaces can provide desired light absorption capability and a fast photoinduced electron transfer and long-live charge-separated state.[18] Recently, we reviewed controlled decoration of macromolecules on various surfaces[19] and studied a unique π-conjugated aromatic compound with butterfly-shape[20,21] which showed interesting thermal and photophysical properties. Click reaction is recognized to be very effective on various azide functionalized surfaces.[22-25] Further, Click reaction produces a unique semi conjugated triazole linker which prevents direct electron transfer through bond so that fullerene and butterfly-shaped molecule

stays as an isolated unit,[26] although electron hopping between them is possible. Hence, as depicted in Scheme 1 (right side), as a synthetic strategy, we performed the click reactions on properly substituted fullerene, containing twelve azide groups,[27] for controlled decoration of fullerenes with butterfly-shaped TBF molecule (denoted as $TBF_{12}C_{60}$). It forms nanoscale self-assembly from DMF solvent due to its unique shape. As depicted in the same scheme (left side), fullerene was also decorated with two TBF units separately (denoted as TBF_2C_{60}) for comparison purposes using a slightly different strategy, where instead of alkyne functionalized TBF, azide functionalized TBF was used. Interestingly, the efficacy of dye degradation increased manifold when $TBF_{12}C_{60}$-ZnO (composite of $TBF_{12}C_{60}$ and ZnO) was used instead of ZnO alone. In contrast, C_{60}-ZnO (composites of C_{60} and ZnO), $Alk_{12}C_{60}$-ZnO (composite of alkyne-functionalized C_{60} and ZnO) or TBF_2C_{60}-ZnO (composite of TBF_2C_{60} and ZnO) shows a marginal increase in efficacy. This unusual increase compared to the isolated components may be attributed to the multivalent effect and two-way electron/hole transitions from/to ZnO and butterfly-shaped TBF compound through fullerene.

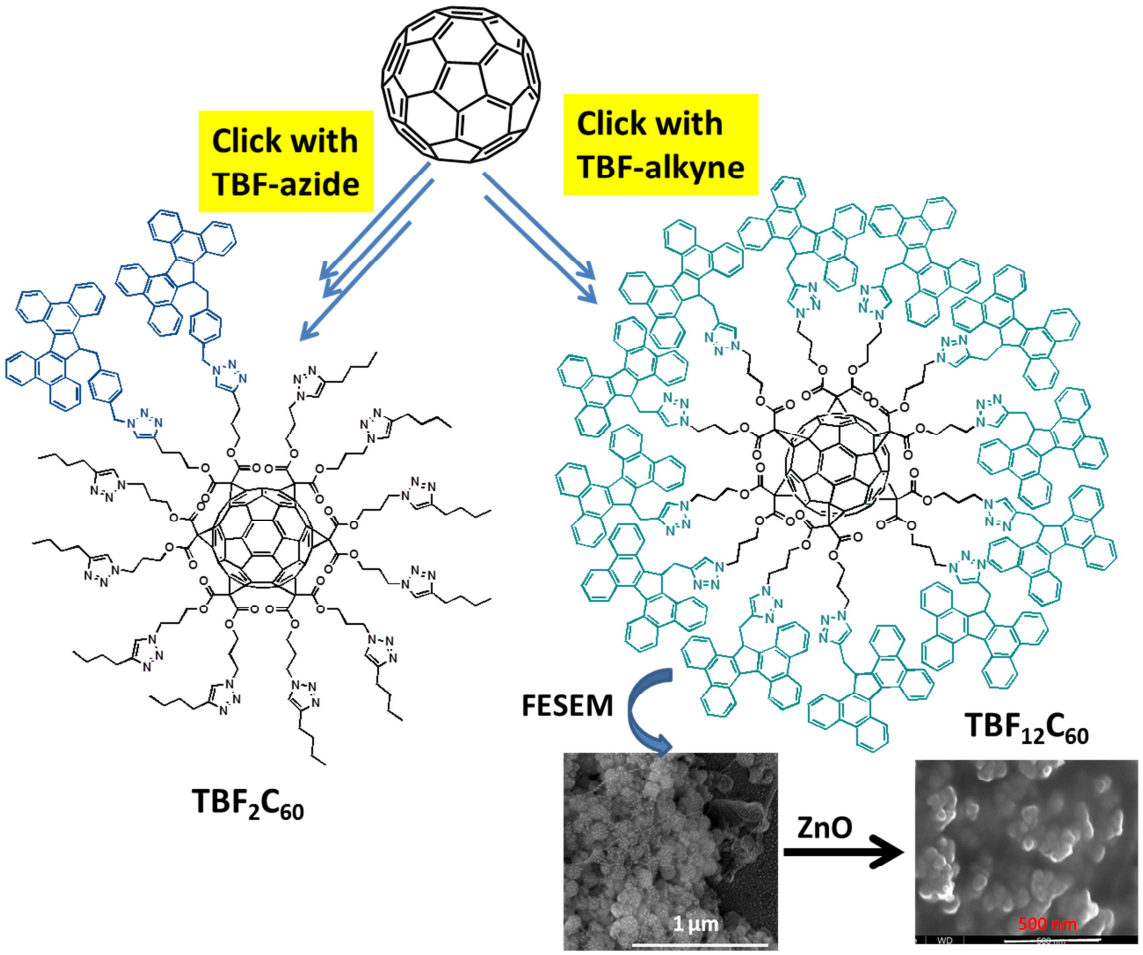

Scheme 1. Synthetic strategies for the controlled decorations of fullerenes with Tetrabenzofluorene (TBF) Moiety. Left side: with two TBF moieties (TBF_2C_{60}); right side: with twelve TBF moieties ($TBF_{12}C_{60}$). Inset: FESEM pictures of $TBF_{12}C_{60}$ alone (left side) and $TBF_{12}C_{60}$-ZnO composite (Right side)

2. RESULTS AND DISCUSSION

2.1. Synthesis and characterization of C_{60}-TBF adducts

As depicted in **Scheme 1**, two different synthetic strategies were followed to separately decorate fullerene with either two units (TBF_2C_{60}) or twelve TBF ($TBF_{12}C_{60}$) units. As depicted in the detailed procedure in ESI, while $TBF_{12}C_{60}$ could be prepared straightaway from azide functionalized C_{60}, a similar strategy did not work for TBF_2C_{60}. Hence it was synthesized first by the differential decoration of fullerene with both azide and triazole units followed by click reaction with alkyne-functionalized TBF. The detailed synthetic procedure for TBF alkyne (alkyne-functionalized TBF), TBF-N_3 (azide-functionalized TBF), $Az_{12}C_{60}$ (C_{60}-functionalized with 12 units of azides), $Alk_{12}C_{60}$ (C_{60} functionalized with 12 units of alkyne), TBF_2C_{60} (C_{60} functionalized with 2 units of TBF), and $TBF_{12}C_{60}$ (C_{60} functionalized with 12 units of TBF) were provided in the Supporting Information (Section S2, ESI). The ^1H, ^{13}C NMR spectra, and MALDI spectra (Section S13, ESI) confirmed the formation of the compounds. The FT-IR spectra of $TBF_{12}C_{60}$ (Figure S17, ESI) showed the characteristic triazole peak at 1496 cm^{-1}. The peak at 3037 cm^{-1} corresponding to the aromatic stretching frequency was also clearly visible. The disappearance of free residual azide groups at 2100 cm^{-1} confirmed a quantitative conversion. Further, ^1H NMR spectra clearly showed the typical triazole proton signal at 5.59 ppm (Figure S33, ESI). This unusual up-field shifting may be attributed to the high aromatic ring current of the TBF molecules. Further, the triazole-attached CH_2 protons appeared at 3.40-3.67 ppm. The aromatic protons were observed between 7.43-8.53 ppm with characteristic peak broadening. In ^{13}C NMR spectra, the expected triazole carbon and carbonyl resonance appeared at 121.1 ppm and 161.4 ppm. Fullerene resonance was observed at 143.8, and 142.8 ppm, and TBF aromatic carbon signals appeared at 143 ppm and 121-136 ppm, respectively (Figure S34, ESI). The UV-Visible absorption and emission spectra of the $TBF_{12}C_{60}$ were measured in DMF (ESI, Figure S7). The typical UV-Visible absorption band for the TBF unit was observed at λ_{max} = 368 nm due to the π–π^* transition. However, the emission of the TBF fragments and absorption of the fullerene with some spectral overlap between 150–400 nm provides a pathway for energy transfer between the donor-acceptor fragments via the FRET mechanism. The UV-Visible absorption and emission spectra of the TBF alkyne, TBF-N_3, $Alk_{12}C_{60}$, TBF_2C_{60} compounds were also measured in DMF and provided in the ESI, (Figure S7, and S8). The ZnO and prepared composites such as C_{60}-ZnO, $Alk_{12}C_{60}$-ZnO, TBF_2C_{60}-ZnO, and $TBF_{12}C_{60}$-ZnO were studied by powder XRD and UV-DRS.

2.2 Transient Absorption Measurements

The photo-induced electron and energy transfer processes were investigated by femtosecond transient absorption analysis (fsTA). The transient absorption spectra of the TBF_2C_{60}, $TBF_{12}C_{60}$ and corresponding decay profiles are shown in Figure 1 and Figure S13, S14. The samples were prepared at 100 μM in DMF and excited at 343 nm. In the case of $TBF_{12}C_{60}$, the $TBF_{12}C_{60}$* excited state (695 nm) is generated and followed by a rapid decay over 12 ± 1 ps and a long decay over 1.79 ± 0.03 ns. The shorter decay is 250-fold faster than the excited-state decay of free TBF-alkyne (ESI, Figure S12), which signifies the role of the fullerene C_{60} in facilitating through-space energy transfer. Indeed, the decay of the TBF* excited state in $TBF_{12}C_{60}$ is associated with the generation of a C_{60}* absorption band at 570 nm. Meanwhile, the absence of new absorption bands could correspond to the charge-separated $TBF^{\bullet+}$ species (verified in situ by spectroelectrochemistry, Figure S10, ESI) in the fsTA spectra of $TBF_{12}C_{60}$ rules out photo-induced electron transfer (PET) in favor of the FRET hypothesis. This is supported with the absence of $C_{60}^{\bullet-}$ in the fsTA spectra, however, the absorption is weak and broad between 700–900 nm (verified in situ by spectroelectrochemistry, Figure S11, ESI), and consequently, this signal could not be easily detected by fsTA. For $TBF_2C_{60,}$ fsTA spectra demonstrates similar features to that of $TBF_{12}C_{60}$ but notably, experience a longer-lived TBF* excited-state over 109 ± 1 ps. Furthermore, C_{60}* has a longer decay of $\tau1$ = 80 ps and $\tau2$ = 1.48 ns for $TBF_{12}C_{60}$ in comparison to TBF_2C_{60} ($\tau1$ = 92 ps and $\tau2$ = 1.07 ns). These data indicate that energy from the TBF* is dissipated faster for the fully decorated $TBF_{12}C_{60}$, either as a result of increased FRET with the fullerene that prolongs the C_{60}* state, or from intramolecular TBF aggregation. Both donor-acceptor hexakis-adducts $TBF_{12}C_{60}$ and TBF_2C_{60} are of similar size and shape, and both are dynamic owing to the hexakis-adduct scaffold that allows for molecular rearrangement. The $TBF_{12}C_{60}$ is highly efficient at absorbing light in the UV-visible region, which is desirable for studying natural light-harvesting systems and designing photo-active functional molecules that have potential applications in photo-active catalysis. The transient absorption spectra and decay profile of TBF-alkyne and $Alk_{12}C_{60}$ were provided in ESI, Figure S12-S15.

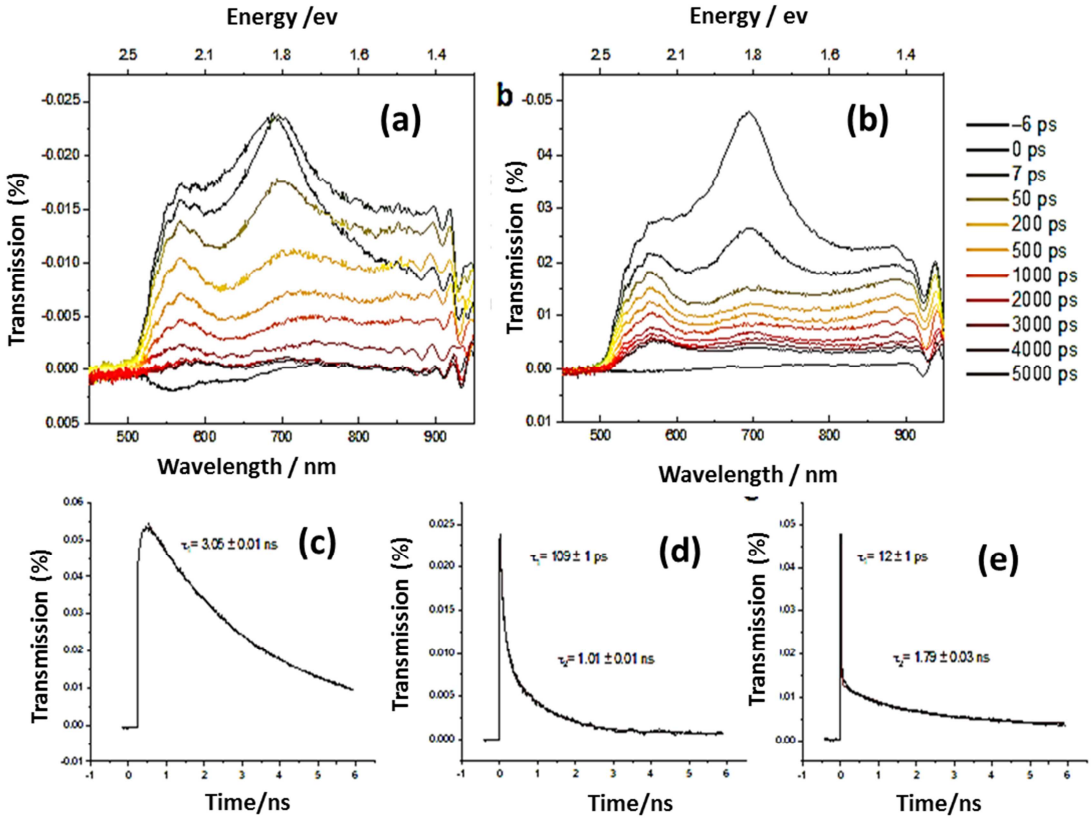

Figure 1. Absorption spectra of (a) TBF_2C_{60} and (b) $TBF_{12}C_{60}$ monitored following pulse at 343 nm. Spectra shown are from pre-pulse (–6 ps) to 5000 ps. Fluorescence Lifetime decay of (c) TBF-alkyne (d) TBF_2C_{60} and (e) $TBF_{12}C_{60}$ measured at 695 nm. Decay is fit to exponential decay.

2.3. Solid-State Optical Properties

The FRET between the TBF units and fullerene core in the solid-state is essential in device fabrications. The photophysical properties of TBF-alkyne, $Alk_{12}C_{60}$, TBF_2C_{60}, and $TBF_{12}C_{60}$ were investigated in thin films, and the data is shown in **Figure 2**. The samples were prepared on quartz substrates at 1 wt% in ZEONEX® from *o*-DCB solutions. Notably, the dispersions at 1 wt% would hone in on mainly intramolecular interactions in the solid state. The absorption band correlating to the TBF units of TBF_2C_{60} shows a redshift to 393 nm (~14 nm), whereas $TBF_{12}C_{60}$ shows a redshift to 396 nm (~ 15 nm) in comparison to when in DMF (Figure 4a), which indicates that there is an increased TBF aggregation around the fullerene scaffold in the solid-state. The absorption for TBF-alkyne (Figure 2a) also bathochromically shifts ($\Delta\lambda_{max}$ = 9 nm, vs DMF) when embedded in the polymer, suggesting some intramolecular TBF aggregation is still facilitated at 1 wt%. In the case of $Alk_{12}C_{60}$ (Figure 2a and 2b), the absorption and emission profile is similar to when solvated by DMF (Figure 2c and 2d), which suggests that $Alk_{12}C_{60}$ is likely in the same (non-aggregated) environment when solvated by DMF and when at 1 wt%. The emission spectrum of $TBF_{12}C_{60}$ (Figure 2b) provides some initial evidence of FRET[29] with a NIR emission at ~ 700 nm. For the TBF_2C_{60}, the NIR emission is observed at ~ 650 nm; however, this is relatively lower in intensity than the TBF centered emission (420 nm). These observations suggest that the hexakis-adduct scaffold facilitates extended TBF

intramolecular aggregation and FRET in the solid-state, which is more pronounced for the fully decorated hexakis-adduct $TBF_{12}C_{60}$. We hypothesized that neat films would allow us to probe the inclusion of extended intermolecular interactions on the energy transfer processes. Neat films of TBF alkyne, $Alk_{12}C_{60}$, TBF_2C_{60} and $TBF_{12}C_{60}$ (Figure 2c and 2d) were prepared similarly to the embedded polymer samples from drop cast solution in DMF [0.1 mg/ mL]. Additionally, a [1:12] mixture of $Alk_{12}C_{60}$ and TBF alkyne was prepared to investigate the effect of tethering the TBF units covalently to the fullerene scaffold. For hexakis-adducts, TBF_2C_{60} and $TBF_{12}C_{60}$ (Figure 2c) show a slight blue shift (~ 8 and ~ 4 nm, respectively) in absorption in contrast to when dispersed in the polymer. This may arise from intermolecular aggregation of TBF units in a slightly thermodynamically destabilizing assembly which is not enforced when in a monodisperse state. A broad and featureless emission (Figure 2d) with significant intensity is observed for $TBF_{12}C_{60}$ at $\lambda_{em,\ max}$ = 650–700 nm, which is similar to the emission profile of $Alk_{12}C_{60}$. In the case of TBF_2C_{60}, the fullerene C_{60} emission was observed with much lower intensity relative to the TBF centered emission at 440 nm. The emission profile (Figure 2d) of the non-covalent mixture $Alk_{12}C_{60}$: TBF alkyne was highly reminiscent of neat TBF alkyne; however, a weak emission at 646 nm from the fullerene C_{60} core is observed. These results indicate that the covalent linkage of the TBF units and the fullerene C_{60} enhances FRET between the TBF units and the fullerene with the ratio between the C_{60} (λem, max =685 nm) and TBF (λem, max =420 nm) emission at 1.13, 0.53 and 0.09 for $TBF_{12}C_{60}$, TBF_2C_{60} and non-covalent mixture $Alk_{12}C_{60}$: TBF alkyne respectively.

Furthermore, the solid-state excitation experiments (Figure S9, ESI) of $TBF_{12}C_{60}$ neat films carried out at 435 nm to produce typical excitation profiles. The morphology of the $TBF_{12}C_{60}$ assemblies was further investigated by HRTEM and AFM (Figure S19-S20, ESI) with the formation of spherical nanostructures observed from drop-caste solutions in DMF. This may be attributed to the π–π stacking of extended assemblies of TBF units attached to the fullerene but decorated in three-dimensional space. This closely packed assembly is essential for efficient electron/hole transfer to facilitate dye degradation under sunlight.

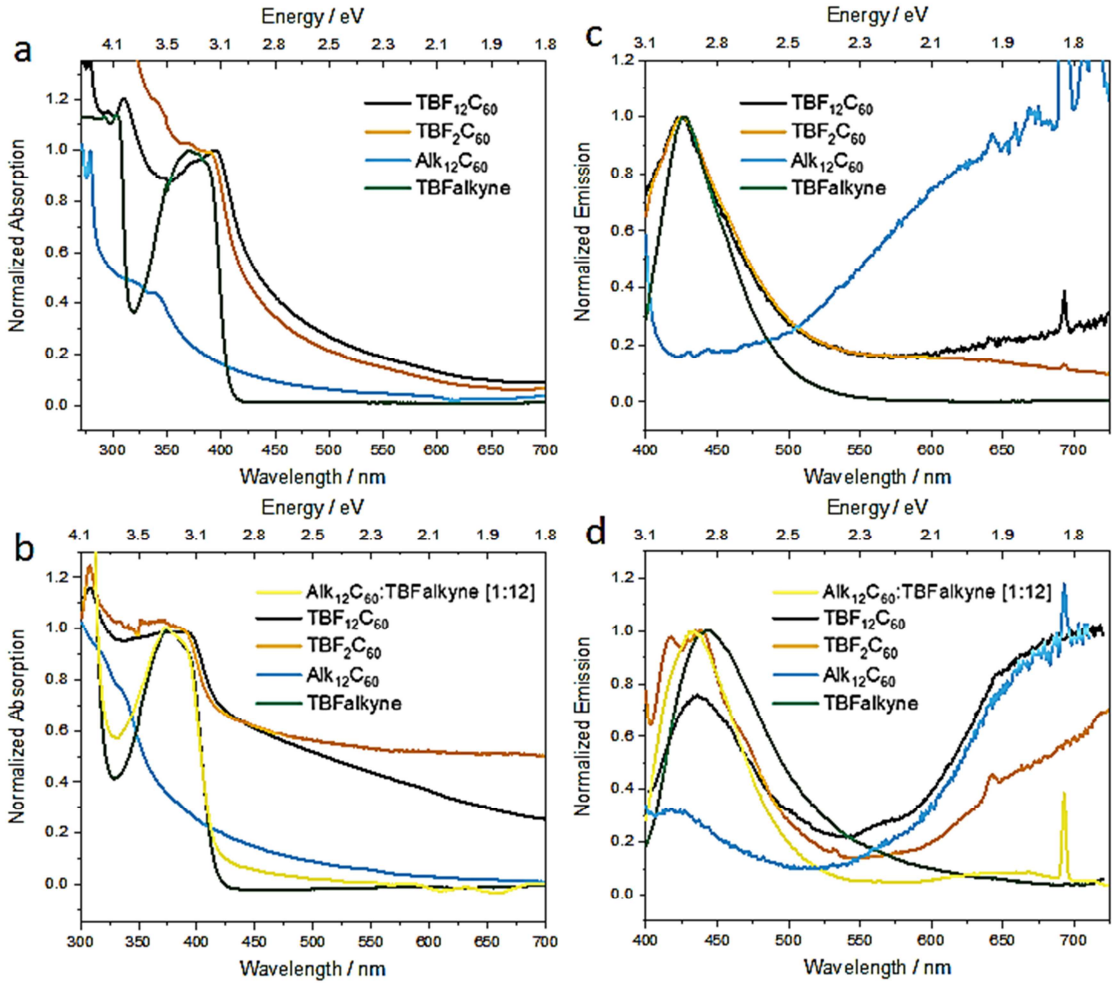

Figure 2. Solid-state UV-Visible spectra of absorption (a) and emission (b) of TBF alkyne, $Alk_{12}C60$, TBF_2C_{60}, and $TBF_{12}C_{60}$ compounds dispersed at 1 wt% in ZEONEX matrix with o-DCB solutions. The Solid-state absorption (c) and emission (d) of thin films of compounds drop cast from solutions of DMF [0.1mg/ mL]. Control non-covalent mixture of $Alk_{12}C_{60}$:TBF alkyne (1:12) (yellow). The emission spectra were collected after excitation at 390 nm in all the cases.

2.4. Electrochemical Properties

The Cyclic voltammograms of TBF alkyne and TBF-N_3 (Figure 3) show two separate oxidation processes at ca. +1.11 V ($TBF^{+\bullet}$) and ca. +1.34 V (TBF^{2+}) in DMF for both compounds. The Cyclic voltammetry (CV) experiments for the TBF_2C_{60} and $TBF_{12}C_{60}$ were also conducted in DMF at 0.2 mM and 0.5 mM, respectively. As identified by UV–Visible spectroscopy, the hexakis-adduct scaffold should facilitate intramolecular TBF aggregation around the periphery of the globular scaffold. The oxidation behavior of TBF_2C_{60} is not dissimilar to TBF alkyne and TBF-N_3, which undergoes two oxidation events at +1.13 and +1.34 V to generate $[TBF_2C_{60}]^{4+}$. However, the voltammogram of $TBF_{12}C_{60}$ provides insight into how intramolecular TBF aggregation[30] can influence the electrochemical properties.

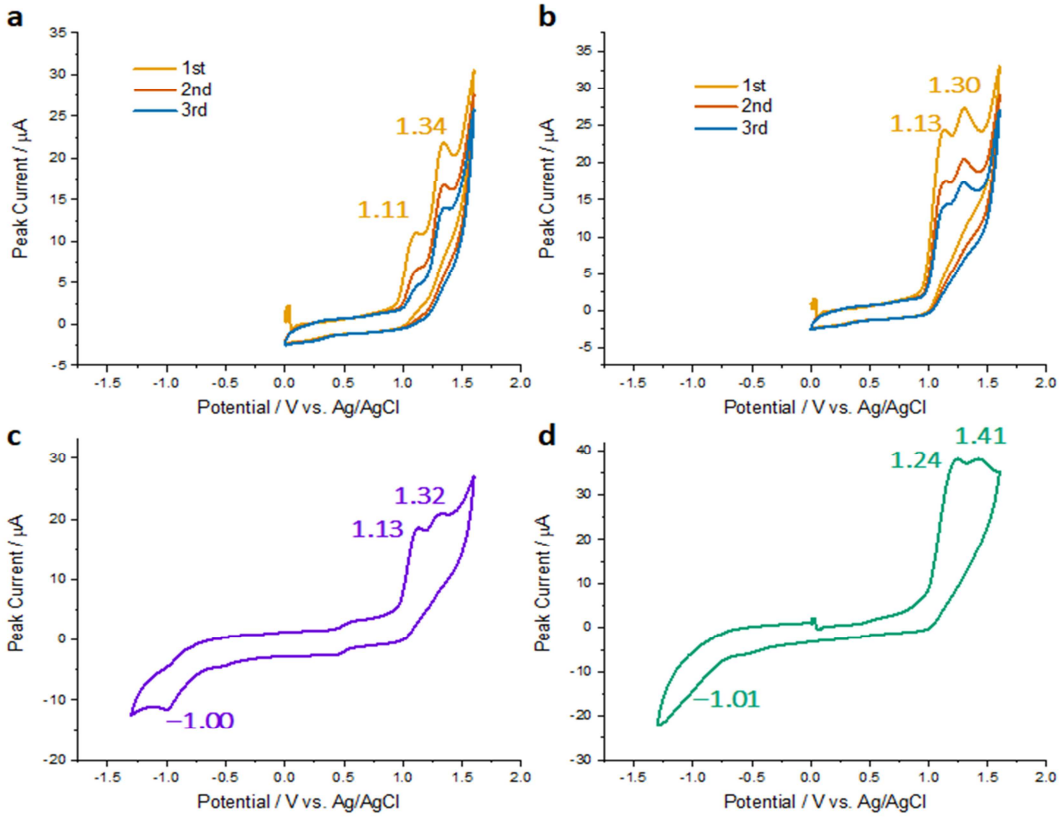

Figure 3. Cyclic voltammogram (100 mVs-1, 298 K) of (a) TBF-Alkyne, (b) TBF-N_3 at [1.0 mM], (c) TBF_2C_{60} [0.5 mM] and (d) $TBF_{12}C_{60}$ [0.2 mM] in degassed DMF containing $TBAPF_6$ [0.1 M], 298 K.

A notable higher oxidation potential (+1.24 V vs. +1.13 V for TBF_2C_{60}) is required to generate the first oxidised species, presumably $TBF_{12}C_{60}^{12(\bullet+)}$. The increased difficulty in oxidation can be rationalized owing to the likely thermodynamically favorable electronic π-couplings between neutral TBF units that are proximal to electron-deficient $TBF^{\bullet+}$ radicals. Indeed, this is further evidenced by an even higher potential (+1.41 V vs. +1.32 V for TBF_2C_{60}) for the full oxidation of each TBF unit forming the fully oxidized $TBF_{12}C_{60}^{24+}$. Additionally, the irreversible reduction of the fullerene C_{60} core is observed at –1.00 and –1.01 V for TBF_2C_{60} and $TBF_{12}C_{60}$, respectively. The HOMO and LUMO of the compounds as unit system were calculated and provided in Table 1. These results indicate the potential multi-redox behavior of $TBF_{12}C_{60}$ and confirm the extended intramolecular aggregation of TBF units around the fullerene scaffold in $TBF_{12}C_{60}$.

Table 1. Electorchemical data for TBF-Alkyne, TBF-N_3, $Alk_{12}C_{60}$, TBF_2C_{60} and $TBF_{12}C_{60}$.

Compound	E_{ox}^{onset} [V]	E_{red}^{onset} [V]	HOMO [eV]	LUMO [eV]	E_{gap}^{opt} [eV]	E_{gap}^{elec} [eV]
TBF-alkyne	0.96 (q) 1.34 (q)	—	–5.22[a]	–2.13	3.09	—
TBF-azide	0.96 (q) 1.30 (q)	—	–5.22[a]	–2.14	3.08	—
$Alk_{12}C_{60}$	–	–0.75 (ir)	–5.56	–3.47	2.09	—
TBF_2C_{60}	0.99 (q) 1.30 (q)	–0.75 (ir)	–5.21	–3.47	2.13	1.74
$TBF_{12}C_{60}$	0.98 (q) 1.42 (q)	–0.77 (ir)	–5.20	–3.45	2.12	1.75

Onset of oxidation and reduction processes were used to calculate HOMO and/or LUMO energies; (q) denotes quasi-reversible process. [a] EHOMO = –(Eox onset – E1/2(Fc/Fc+) +4.75) eV, [b] ELUMO = –(Ered onset – E1/2(Fc/Fc+) +4.75) eV, [c] ELUMO = –(HOMO [eV] + Egapopt [eV]) eV, [d] calculated using onsent of absorption, [e] ELUMO–EHOMO eV.

2.5. XRD Studies. Powder X-ray diffraction (PXRD) patterns were collected to probe any change to ZnO crystalline structure and size upon composite formation with the data shown in Figure 4A. For ZnO, the well-established (100), (002), (101), (102), (110), (103), (200), (112), (201), (004), (202) crystal planes of its hexagonal lattice geometry were observed.[31] The diffraction patterns are relatively unchanged for the C_{60}-ZnO, $Alk_{12}C_{60}$-ZnO, TBF_2C_{60}-ZnO, and $TBF_{12}C_{60}$-ZnO composites, suggesting no significant change to the crystalline structure of ZnO following composite preparation. The ZnO particle size was calculated using the Debye–Scherer equation for each composite using $2\theta = 35.9$. The crystallite sizes were found to be 30.4, 32.6, 30.1, 29.0, and 31.4 nm for ZnO, C_{60}-ZnO, $Alk_{12}C_{60}$-ZnO, TBF_2C_{60}-ZnO, and $TBF_{12}C_{60}$-ZnO, respectively, confirming that the preparation of the composites did not alter ZnO particle sizes. Furthermore, the similar crystallite sizes demonstrate that the surface area of the ZnO nanoparticles was a similar size, and therefore the number of reactive sites available for dye degradation processes could be the same throughout, and changes in photo-catalytic efficacy directly correlated to the organic dopant. In all the cases, the C_{60} diffraction peaks were not observed because of the low content of C_{60} in the composite. After composition, the SEM images showed that the $TBF_{12}C_{60}$ was well dispersed with ZnO and uniformly covered on ZnO with spherical aggregates (ESI, Figure S21), which provides more reactive sites for efficient dye degradation.

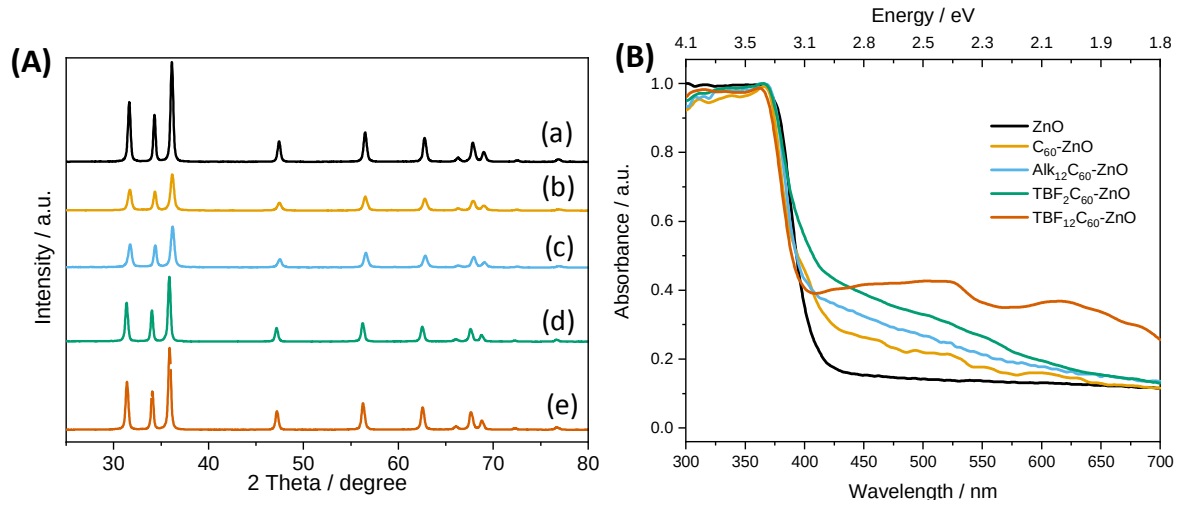

Figure 4. (A) XRD spectra of ZnO (a), C_{60}-ZnO (b), $Alk_{12}C_{60}$-ZnO (c), TBF2 C_{60}-ZnO (d) and $TBF_{12}C_{60}$ZnO (e). (B) UV-Vis diffuse reflectance spectra of ZnO, C_{60}ZnO, TBF_2C_{60}-ZnO, $Alk_{12}C_{60}$-ZnO and $TBF_{12}C_{60}$-ZnO composite

2.6. UV-Visible diffuse-reflectance spectroscopy (DRS)

UV-Visible DRS studies investigated the optical behavior and bandgap of the composite materials, and the data is shown in Figure 4B. The ZnO alone shows a strong absorption at ca. 400 nm with a bandgap of 3.08 eV; this is similar to that previously reported for ZnO nanoparticles. For the C_{60}-ZnO and $TBF_{12}C_{60}$-ZnO, the apparent bandgap was slightly increased to 3.14 and 3.19 eV, respectively. The blue shift in the absorption of the composites could be evidence of Burstein–Moss (BM) effect[32] and indicate that the properties of ZnO are significantly modified even at 1 wt% towards efficient dye degradation of different organic dyes. Moreover, the presence of fullerene in the composite can act as an energy sensitizer, potentially increasing the high charge transfer and photo-catalytic quantum efficiency. The materials bandgap was calculated using Tauc plots and provided in Figure S18, ESI.

2.7. Photocatalytic Performance

We envisaged that $TBF_{12}C_{60}$ would enhance the photocatalytic efficiency of ZnO by participating in redox reactions that prevent recombination of h^+ and e^- on ZnO, which are ultimately sites for the generation of degrading radical species such as $^{\bullet}OH$ and $O_2^{\bullet-}$. The photocatalytic activity of the $TBF_{12}C_{60}$-ZnO composite was examined by degrading Rhodamine B (RhB) dye in an aqueous solution under a sunlight irradiation source. All composites were tested with 1 wt % of dopant and plotted in Figure 5(a). As observed from Figure 5(a), degradation efficiency is greater for the dye tested for $TBF_{12}C_{60}$-ZnO composites in comparison to neat ZnO, C_{60}-ZnO, $Alk_{12}C_{60}$-ZnO, and TBF_2C_{60}-ZnO composites. Particularly, as observed from Figure 5(a), the concentration of 12 ppm of RhB showed more than 80 % dye degradation in two hours using $TBF_{12}C_{60}$-ZnO. For the control composites such as ZnO, C_{60}-ZnO, $Alk_{12}C_{60}$-ZnO, and Alk_2C_{60}-ZnO composites, there were 30%, 55%, 60% and 52% dye degradation respectively, under the same conditions (at 12 ppm). The results were provided in Table S1.

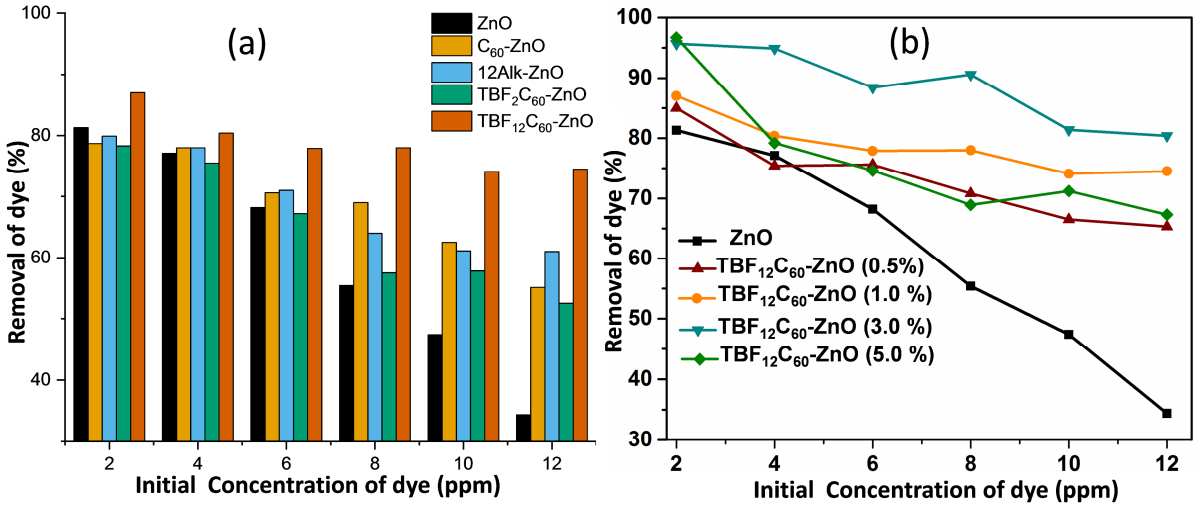

Figure 5. Photocatalytic degradation of RhB using (a) ZnO, C_{60}-ZnO, $Alk_{12}C60$-ZnO, TBF_2C60-ZnO and $TBF_{12}C_{60}$-ZnO composites, (b) The degradation of RhB using $TBF_{12}C_{60}$-ZnO composite at varying wt% loading of $TBF_{12}C_{60}$.

In order to optimize the performance of the $TBF_{12}C_{60}$-ZnO composite, various loading (weight %) of $TBF_{12}C_{60}$-ZnO were explored. At the lowest starting concentration of RhB dye (2 ppm), there is an improvement in performance for the 3.0 wt% and 5.0 wt% composites, with 96% and 97% removal of dye, respectively (Figure 5(b)). The photo-catalytic performance decreases with excessive amounts of $TBF_{12}C_{60}$-ZnO as direct irradiation to ZnO is diminished with $TBF_{12}C_{60}$-ZnO covering the surface and forming large, light-absorbing aggregates. The results were provided in Table S2.

To quantify the rate of dye degradation for the best performing composite, the removal of RhB from the solution was monitored over time using the 3 wt% composites. A solution of RhB (12 ppm) was mixed with 3 wt% $TBF_{12}C_{60}$-ZnO composites, and aliquots were taken every 30 minutes (for 180 minutes) with the concentration of dye remaining calculated by UV-Vis spectroscopic measurements. The results were provided in Table S3. As observed from Figure 6(a) at concentrations of 12 ppm, the photo-catalyst $TBF_{12}C_{60}$-ZnO shows almost complete degradation of RhB within 3 hours of sunlight irritations. For the TBF_2C_{60}-ZnO composites case, the dye solution was not completely degraded, with the percentage of dye removal calculated to be 64%. The kinetics studies were performed to calculate the reaction rate of the photocatalytic degradation of RhB assuming a pseudo-first-order equation and shown in Figure 6 (b). The rate constant (k) values for the degradation of RhB over the TBF_2C_{60}-ZnO and $TBF_{12}C_{60}$-ZnO were found to be 5.01×10^{-3} min^{-1} and 1.5×10^{-2} min^{-1} respectively (measured using the standard curve as details provided in ESI, section S12.5, equation 2). The rate constant for $TBF_{12}C_{60}$-ZnO was higher than that of pristine ZnO and other control composites rate constants (ESI Table S4). These results prove the high photocatalytic performance of $TBF_{12}C_{60}$-ZnO enhanced by incorporating the dodeca-substituted fullerene. The kinetic data is provided in Tables S4a and S4b. Further, to demonstrate the diverse use of the $TBF_{12}C_{60}$-ZnO composite, the degradation studies were conducted on a range of industrially relevant dyes such as

Reactive Blue 4 (RB4, 50 ppm), Quinoline Yellow (QY, 12 ppm), Methylene Blue (MB, 20 ppm) and Safranin (SO, 20 ppm); all degradation was monitored by UV-Vis spectroscopy (Figure S24) under similar conditions as the RhB degradation experiments and compared against the degradation using neat ZnO. Although the concentration is varied for each dye, the $TBF_{12}C_{60}$-ZnO composite consistently outperforms (Figure 7a) neat ZnO. Indeed, for MB, the $TBF_{12}C_{60}$-ZnO composite approaches near 100% removal of dye from solution, compared to just 64 % for ZnO. The efficient photocatalytic performance of $TBF_{12}C_{60}$-ZnO photocatalyst was demonstrated against organic dye compounds (SO, RB4, QY) that differ significantly in the chemical structure.

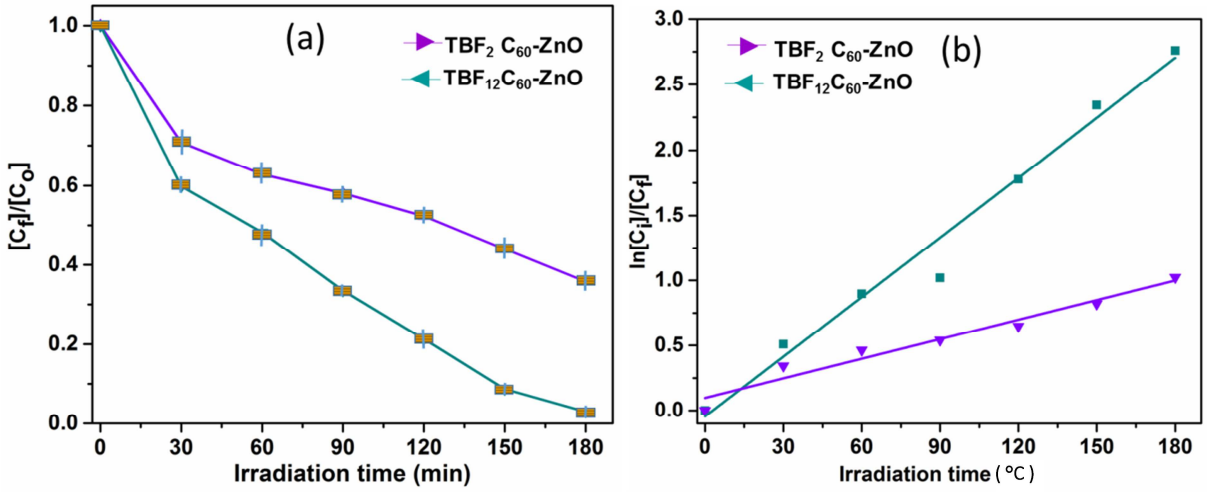

Figure 6. (a) Photocatalytic degradation of RhB using photocatalyst (time variation), (b) Kinetic plot of RhB dye degradation with TBF_2C_{60}-ZnO and $TBF_{12}C_{60}$-ZnO photocatalyst.

2.8. Recyclability in photocatalysis: In order to test the recyclability of the $TBF_{12}C_{60}$-ZnO composite (Figure 7b), we performed multiple dye degradation experiments with a single batch of 3 wt% $TBF_{12}C_{60}$-ZnO composites on fresh RhB (12 ppm) solutions. The 3 wt% $TBF_{12}C_{60}$-ZnO composites showed an efficacy of 80% for the first dye degradation experiment. After 5 cycles, 62% of dye was still removed from the solution by the composite, which is 77% reproducible compared to the efficacy of the first experiment. This high level of reproducibility serves $TBF_{12}C_{60}$-ZnO as a genuine candidate for a hybrid photo-catalyst with high efficacy. The recyclability results were provided in Table S5.

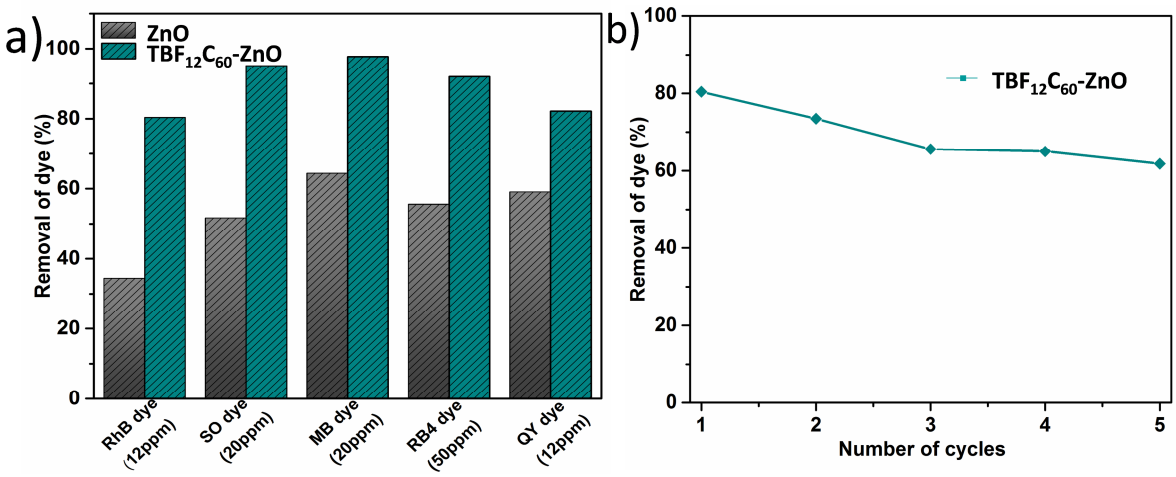

Figure 7. (a) Bar chart shows a comparison between the ZnO and $TBF_{12}C_{60}$-ZnO photocatalyst on different dye compounds degradation. (b) Recycle photo-catalytic performance of $TBF_{12}C_{60}$-ZnO composite.

2.9. Possible mechanism of the enhanced photoreactivity using $TBF_{12}C_{60}$-ZnO

Based on the above results, the possible photocatalytic mechanism for $TBF_{12}C_{60}$-ZnO photo-catalyst is depicted in Figure 8. The donor-acceptor hybrid of $TBF_{12}C_{60}$ is bestowed with oxidative as well as reductive units. We presumed that TBF and fullerene units of $TBF_{12}C_{60}$ behave as distinctly separate entities (confirmed by CV and UV data) and act like "cascade" type systems to facilitate energy transfer during photocatalysis. Cho et al. have explained the electron transfer from fullerene C_{60} to metal oxide such as TiO_2 since "the energy difference between the lowest unoccupied molecular orbital (LUMO) energy level of PCBM and the conduction band of TiO_2 is enough for efficient electron transfer from PCBM to TiO_2".[33] The similar mechanism may be used to explain the electron transfer process between fullerenes C_{60} to ZnO, since our photo-catalyst behaving as separate entities. It is postulated that initially, the energy transfer from TBF units (HOMO is -5.22 and LUMO is -2.13 eV) to fullerene C_{60} core (HOMO is -5.56 and LUMO is -3.45 eV) occurred via the FRET process. At the same time, an exciton is generated and dissociated into electrons and holes in fullerene and ZnO under sunlight irradiation. Then the electron transferred from LUMO of the fullerene C_{60} to the conduction band of ZnO (conductance band is – 4.1 eV) might happen. It is further presumed that the direct energy transfer from TBF to ZnO is also possible. Furthermore, h^+ transfer from the donor TBF units to the fullerene core (i.e., the fullerene HOMO) can happen, which itself provides a pathway for hole hopping between TBF units. Hence, the recombination of photogenerated h^+ and e^- on ZnO and fullerene could be significantly reduced. Subsequently, the concentration of effective radical species (i.e., $O2^{\bullet-}$, $^{\bullet}OH$, H_2O_2) at the surface of ZnO is increased, which ultimately results in greater dye removal from the solution. On the other hand, the TBF_2C_{60}-ZnO composite, which showed 52% efficacy for the degradation of RhB in comparison to $TBF_{12}C_{60}$-ZnO (85%), indicates a possible multivalent effect, responsible for the increased photocatalytic performance.

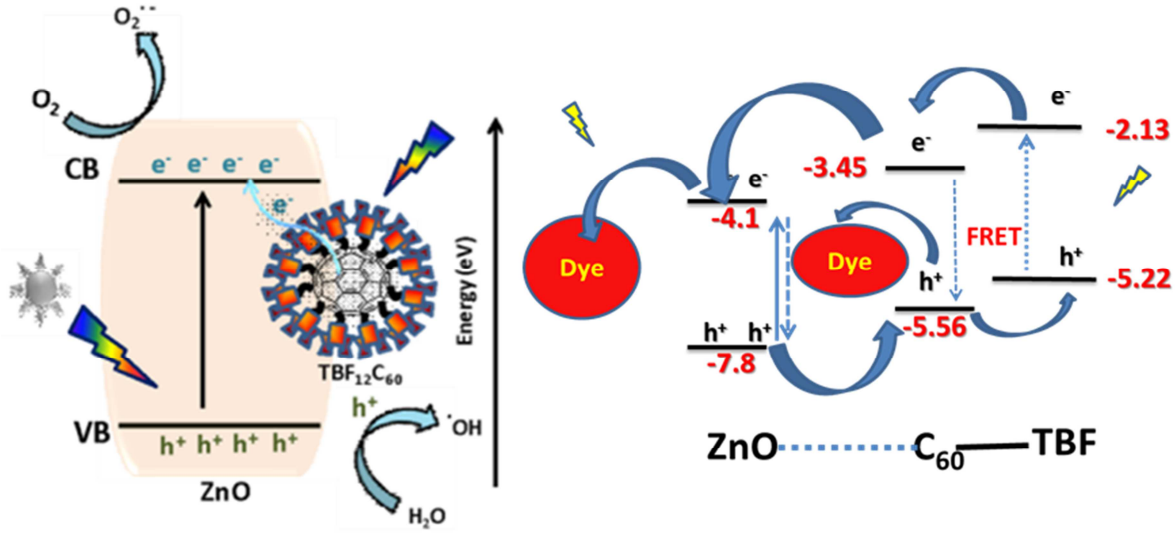

Figure 8. Schematic representation of possible photocatalysis mechanism of $TBF_{12}C_{60}$-ZnO and charge transfer in ZnO/$TBF_{12}C_{60}$ composite under sunlight irradiation.

3. EXPERIMENTAL SECTION

3.1 Materials and methods

All reagents and solvents were purchased from commercial suppliers (Merck, Acros Organics, Alfa Aesar, Fischer Scientific, Tokyo Chemical Industry,or Fluorochem) and used without further purification unless stated otherwise. Anhydrous solvents were obtained from a solvent purification system (neutral alumina) and stored over activated (>250 °C at 0.01 mbar overnight) 3 Å molecular sieves under a dry Ar atmosphere. Solvents and solutions required for air-sensitive manipulations were degassed thoroughly using a minimum of three freeze–pump–thaw cycles and the flask back-filled under a nitrogen atmosphere. TBF-alkyne[20], azidofullerene hexakis-adducts $Az_{12}C_{60}$[27], and $Az_{10}C_{60}$[28] were synthesized using slightly modified previously published literature procedures. The general procedure for Cu (I)-catalyzed azide-alkyne click reaction was described in S2.6, ESI. The single crystal of synthesized TBF-N_3 was achieved by slow evaporation of a mixture of CH_2Cl_2–hexanes and which showed a molecular pack in a pseudo-herringbone array. The crystal data was discussed in Figure S3, ESI. The preparation of ZnO and composites such as C_{60}-ZnO, $Alk_{12}C_{60}$-ZnO, TBF_2C_{60}-ZnO, and $TBF_{12}C_{60}$-ZnO were provided in ESI. Further, the systematic procedure for the photo-catalyst experiment for the efficient dye degradation studies was provided in ESI (Section S12, ESI). The recyclability of the photo-catalyst $TBF_{12}C_{60}$-ZnO composite was performed with multiple cycles and discussed in Figure 7 and ESI, Table S5. All the details about apparatus and instruments are provided in Section S1, ESI.

4. CONCLUSION

Click reactions were successfully used to covalently immobilize butterfly-shaped polycyclic aromatic extended conjugated TBF having either two (mono adduct) or twelve units (hexakis adduct) of

molecule in a controlled manner. Single-crystal X-ray analysis data clearly established the structure and long-range regular packing of TBF part, plausibly helping to create a unique pattern in the self-assembly process of the fullerene-TBF conjugate. UV-Vis spectroscopic and CV studies clearly indicated that due to the presence of triazole/alkyl chain spacers; the TBF and fullerene units are behaving as distinctly separate entities rather than as a unity system. Pulse UV and fluorescence lifetime experiments are clearly showing a FRET process between fullerene and TBF units, which was better when twelve units are immobilized rather than two units. Based on this assumption, and calculation of band gaps from CV and UV data indicated a possibility of a "cascade" type system to facilitate energy transfer during photocatalysis. This was supported by the fact that in some cases photocatalysis was manifold better for TBF-fullerene conjugates rather than only fullerene in presence of ZnO. This finding, particularly the role of TBF as a cascade, should also be useful for other types of photocatalysis or photovoltaics where initial stages like sunlight absorption and exciton generations have a similar mechanism. Further studies in that direction may be taken in the future.

ASSOCIATED CONTENT

Supporting Information†

Synthetic procedures; crystal data; FT-IR spectra; NMR spectra; UV-visible /PL spectra; mass spectra; electrochemical data; FE-SEM and HR-TEM images; dye degradation under various conditions are provided in ESI.

AUTHOR INFORMATION (EMAIL ADDRESS)

Munusamy Krishnamurthy: krishna.che007@gmail.com

Philip A. Hope: philip.a.hope@durham.ac.uk

P. Ramar: ppramar93@gmail.com

A.A. Boopathi: aaboopathichem@gmail.com

Marc K. Etherington: marc.k.etherington@northumbria.ac.uk

Notes. The authors declare no competing financial interest.

ACKNOWLEDGEMENTS

The first author acknowledges INSPIRE PROGRAMME of DST, Government of India, for the financial support in the form of a Senior Research Fellowship (IF130992). Funding from the Newton-Bhabha Ph.D. placement program (British Council, UK, and DST, India) is gratefully acknowledged. M. K. E. would like to thank the EU's Horizon 2020 research and innovation programme for funding the HyperOLED project under grant agreement No. 732013. CSIR-CLRI communication No. is 1645.

References

1. Lee, G. J.; Manivel, A.; Batalova, V.; Mokrousov, G.; Masten, S.; Wu, J. Mesoporous Microsphere of ZnS Photocatalysts Loaded with CuO or Mn3O4 for the Visible-Light-Assisted Photocatalytic Degradation of Orange II Dye. Ind. Eng. Chem. Res. 2013, 52, 11904-11912.
2. Saidi N. M.; Omar F. S.; Numan A.; Apperley D. C.; Algaradah M. M.; Kasi R.; Avestro A.-J.; Subramaniam R. T., Enhancing the Efficiency of a Dye-Sensitized Solar Cell Based on a Metal Oxide Nanocomposite Gel Polymer Electrolyte. Appl. Mater. Interfaces 2019, 11, 30185-30196.
3. Olaru, N.; Calin, G.; Olaru, L. Zinc Oxide Nanocrystals Grown on Cellulose Acetate Butyrate Nanofiber Mats and Their Potential Photo-catalytic Activity for Dye Degradation. Ind. Eng. Chem. Res. 2014, 53, 17968-17975.
4. Adnan, M. A. M.; Julkapli, N. M.; Hamid, S. B. A. Review on ZnO hybrid photo-catalyst: impact on photo-catalytic activities of water pollutant degradation. Rev. Inorg. Chem. 2016, 36, 77-104.
5. Malekshoar, G.; Pal, K.; He, Q.; Yu, A. P.; Ray, A. K. Enhanced Solar Photocatalytic Degradation of Phenol with Coupled Graphene-Based Titanium Dioxide and Zinc Oxide. Ind. Eng. Chem. Res. 2014, 53, 18824-18832.
6. Singh, N.; Prakash, J.; Gupta, R. K. Design and engineering of high-performance photo-catalytic systems based on metal oxide-graphene-noble metal nanocomposites. Mol. Syst. Des. Eng. 2017, 2, 422-439.
7. Zhou, L.; Zhang, H. Y.; Sun, H. Q.; Liu, S. M.; Tade, M. O.; Wang, S. B.; Jin, W. Q. Recent advances in non-metal modification of graphitic carbon nitride for photocatalysis: a historic review. Catal. Sci. Technol. 2016, 6, 7002-7023.
8. Das, R.; Vecitis, C. D.; Schulze, A.; Cao, B.; Ismail, A. F.; Lu, X. B.; Chen, J. P.; Ramakrishna, S. Recent advances in nanomaterials for water protection and monitoring. Chem. Soc. Rev. 2017, 46, 6946-7020.
9. Murugan P.; Ramar P.; Mandal A. B.; Samanta D. Investigating the Photocatalytic Performances of Nanocomposites Containing Narrow-band-gap Copolymers and ZnO. *ChemistrySelect* 2019, 4, 14214-14221.
10. He, Z.; Xiao, B.; Liu, F.; Wu, H.; Yang, Y.; Xiao, S.; Wang, C.; Russell, T. P.; Cao, Y. Single-junction polymer solar cells with high efficiency and photovoltage. Nature Photonics 2015, 9, 174-179.
11. Murugan, P.; Raghavendra, V.; Chithiravel, S.; Krishnamoorthy, K.; Mandal, A. B.; Subramanian, V.; Samanta, D. Experimental and Theoretical Investigations of Different Diketopyrrolopyrrole-Based Polymers. ACS Omega 2018, 3, 11710-11717.
12. Speller, E. M. The significance of fullerene electron acceptors in organic solar cell photo-oxidation. J. Mater. Sci. Technol. 2017, 33, 924-933.
13. Wang, S. Y.; Liu, C. W.; Dai, K.; Cai, P.; Chen, H.; Yang, C. J.; Huang, Q. Y. Fullerene C-70-TiO2 hybrids with enhanced photo-catalytic activity under visible light irradiation. J. Mater. Chem. A, 2015, 3, 21090-21098.
14. Ramar P.; Aishwarya B. V.; Samanta D., A photo-catalytic chip inspired from the photovoltaics of polymer-immobilized surfaces: self-assembly and other factors. *Chem. Commun.* 2021, *57*, 12964-12967.
15. Meng, Z. D.; Ghosh, T.; Zhu, L.; Choi, J. G.; Park, C. Y.; Oh, W. C. Synthesis of fullerene modified with Ag2S with high photo-catalytic activity under visible light. J. Mater. Chem. 2012, 22, 16127-16135.
16. Fu, H. B.; Xu, T. G.; Zhu, S. B.; Zhu, Y. F. Photocorrosion Inhibition and Enhancement of Photocatalytic Activity for ZnO via Hybridization with C-60. Environ. Sci. Technol. 2008, 42, 8064-8069.
17. Moor, K. J.; Valle, D. C.; Li, C. H.; Kim, J. H. Improving the Visible Light Photoactivity of Supported Fullerene Photocatalysts through the Use of C-70 Fullerene. Environ. Sci. Technol. 2015, 49, 6190-6197.
18. Yan, W. B.; Seifermann, S. M.; Pierrat, P.; Brase, S. Synthesis of highly functionalized C-60 fullerene derivatives and their applications in material and life sciences. Org. Biomol. Chem. 2015, 13, 25-54.
19. Murugan, P.; Krishnamurthy, M.; Jaisankar, S. N.; Samanta, D.; Mandal, A. B. Controlled decoration of the surface with macromolecules: polymerization on a self-assembled monolayer (SAM). Chem. Soc. Rev. 2015, 44, 3212-3243.

20. Sampath, S.; Boopathi, A. A.; Mandal, A. B. "Bottom-up" self-assembly and "cold crystallization" of butterfly shaped tetrabenzofluorene molecules. Phys. Chem. Chem. Phys. 2016, 18, 21251-21258.
21. Sturala, J.; Etherington, M. K.; Bismillah, A. N.; Higginbotham, H. F.; Trewby, W.; Aguilar, J. A.; Bromley, E. H. C.; Avestro, A. J.; Monkman, A. P.; McGonigal, P. R. Excited-State Aromatic Interactions in the Aggregation-Induced Emission of Molecular Rotors. J. Am. Chem. Soc. 2017, 139, 17882-17889.
22. Kolb, H. C.; Finn, M. G.; Sharpless, K. B. Click chemistry: Diverse chemical function from a few good reactions. Angew. Chem. Int. Ed. 2001, 40, 2004-2021.
23. Taskin, O. S.; Yilmaz, G.; Yagci, Y. Fullerene-Attached Polymeric Homogeneous/Heterogeneous Photoactivators for Visible-Light-Induced CuAAC Click Reactions. ACS Macro Letters 5, 103-107.
24. Krishnamurthy, M.; Krishnamoorthy, K.; Arulkashmir, A.; Raghavendra, V.; Murali, A.; Jaisankar, S. N.; Murugan, P.; Gurusamy-Thangavelu, S. A.; Nasar, A. S.; Mandal, A. B.; Samanta, D. "Click" polymerization: A convenient strategy to prepare designer fullerene materials. Mater. Des. 2016, 108, 34-41.
25. Samanta, D.; Murugan, P.; Ananthakrishnan, S. J.; Somanathan, N.; Das, S. K.; Jaisankar, S. N.; Mandal, A. B. "Click" polymerization on a self-assembled monolayer: a convenient approach to functionalize various surfaces with polytriazoles. Chem. Commun. 2012, 48, 12068-12070.
26. de Miguel, G.; Wielopolski, M.; Schuster, D. I.; Fazio, M. A.; Lee, O. P.; Haley, C. K.; Ortiz, A. L.; Echegoyen, L.; Clark, T.; Guldi, D. M. Triazole Bridges as Versatile Linkers in Electron DonorAcceptor Conjugates. J. Am. Chem. Soc. 2011, 133, 13036-13054.
27. Iehl, J.; de Freitas, R. P.; Delavaux-Nicot, B.; Nierengarten, J. F. Click chemistry for the efficient preparation of functionalized 60 fullerene hexakis-adducts. Chem. Commun. 2008, 2450-2452.
28. Iehl, J.; Nierengarten, J.-F. A Click–Click Approach for the Preparation of Functionalized [5:1]-Hexaadducts of C60. Chem. Eur. J 2009, 15, 7306-7309.
29. Jones, G. A.; Bradshaw, D. S. Resonance energy transfer: from fundamental theory to recent applications. Front. Phys. 2019, 7, 100.
30. Yoosaf, K.; Iehl, J.; Nierengarten, I.; Hmadeh, M.; Albrecht-Gary, A.-M.; Nierengarten, J.-F.; Armaroli, N. A supramolecular photosynthetic model made of a multiporphyrinic array constructed around a C60 core and a C60-imidazole derivative. Chem. Eur. J 2014, 20, 223-231.
31. Murali, A.; Sohn, H. Photocatalytic properties of plasma-synthesized aluminum-doped zinc oxide nanopowder. J. Nanosci. Nanotechnol. 2019, 19, 4377-4386.
32. Tang, G.; Liu, H.; Zhang, W. The variation of optical band gap for ZnO: In films prepared by sol-gel technique. Adv. Mater. Sci. Eng. 2013, 2013.
33. Cho, E.-C.; Ciou, J.-H.; Zheng, J.-H.; Pan, J.; Hsiao, Y.-S.; Lee, K.-C.; Huang, J.-H. Fullerene C70 decorated TiO2 nanowires for visible-light-responsive photo-catalyst. Appl. Surf. Sci. 2015, 355, 536-546.